

Influence of capillary viscous flow on melting dynamics

Michael Blank^a, Prapanch Nair^{a,*}, Thorsten Pöschel^a,

^a *Institute for Multiscale Simulation, Friedrich-Alexander Universität Erlangen-Nürnberg, Erlangen.*

Abstract

The rate of melting of a solid and the rate of deformation of the resulting melt due to capillary forces are comparable in additive manufacturing applications. This dynamic structural change of a melting solid is extremely challenging to study experimentally. Using meshless numerical simulations we show the influence of the flow of the melt on the heat transfer and resulting phase change.

We introduce an accurate and robust Incompressible Smoothed Particle Hydrodynamics method to simulate melting of solids and the ensuing fluid-solid interaction. We present validation for the heat transfer across free surface and the melting interface evolution, separately. We then present two applications for this coupled multiphysics simulation method—the study of rounding of an arbitrarily shaped particle during melting and the non-linear structural evolution of three spheres undergoing agglomeration. In both the studies we use realistic transport and thermal properties for the materials so as to demonstrate readiness of the method for solving engineering problems in additive manufacturing.

Keywords: Additive manufacturing, Incompressible Smoothed Particle Hydrodynamics, phase change, latent heat, melting dynamics

1. Introduction

The evolution of topology in melting system, such as encountered in additive manufacturing applications, is often studied by decoupling the time scales of the flow of the melt and the phase change. Either static material properties are assumed, approximating the solids as highly viscous fluids [7] or assuming no flow following melting [21]. As the scope of additive manufacturing widens, there is an increasing need to resolve the tight coupling between flow of the melt and the phase change in order to achieve expected strength of the material. For serious engineering applications, uniformity in density and strength of the manufactured

*Principal corresponding author

Email address: `prapanch.nair@fau.de` (Prapanch Nair)

parts demand a micro mechanical understanding of the structural evolution during successive melting and solidification the material undergoes several times. Experimental studies at such spatial and temporal resolutions may be expensive [4], not to mention the high temperature conditions in which measurements need to be made. Traditional numerical approaches based on mesh based methods (Finite Volume Method, Finite Element Method) are often challenged by complex geometry evolutions; this is inherently due to the need to maintain the neighbor connectivity information between the computational nodes. Meshless methods hold several advantages for such multi-physics applications.

Smoothed Particle Hydrodynamics (SPH) is a meshfree updated-Lagrangian method which was introduced by Ginghold and Monaghan [3] and Lucy [10] for treating astrophysical phenomena and gas dynamics. Since the method is free from the need for the mesh connectivity information, many problems with complex interfaces and discontinuities in the domain are effectively solved by the method, making it a practical tool for multiphysics problems. For example, Monaghan presented an impressive SPH simulation of a methane gas bubble toppling a trawler to explain the sinking of ships in Witches Hole in the North sea [11]. This multiphysics simulation coupled two phase flow with free surface to an interacting rigid body. Heat transfer [14], phase change [2], and capillary flows [15] are solved separately using the method and are being continuously applied to a wide variety of engineering problems.

To successfully couple heat transfer, phase change and capillary flows in the context of additive manufacturing applications, each of these modules need to be improved and validated for appropriate boundary conditions (BC). Heat transfer is solved in SPH using the passive scalar approach for temperature [14]. The definition of accurate second order derivatives with discontinuous transport coefficients makes it applicable to realistic problems. Heat transfer from an ambient constant (or time varying) temperature needs to be implemented as a Dirichlet BC for temperature. A thin layer of particles may be used for such BCs, but this would deteriorate the order of accuracy of the method itself. Hence, for problems undergoing continuous deformation, we present a free surface Dirichlet BC that is quite similar to the free surface Dirichlet BC for pressure in an earlier work [16].

The transport of passive scalar—through convection due to capillary flow and conduction—causes phase change based on the latent heat capacity of the material. Using SPH, static phase change has been solved [2] using fixed particles for boundaries. Enthalpy based formulations have also been used for solving heat transfer in SPH [2] as an alternative approach. However these involve computations of higher order derivatives than the temperature based approach. Capillary forces can be implemented in SPH using either continuum surface force based models, geometric reconstruction of the interfaces or using pairwise potential forces. For free surfaces we find the potential forces to be more amenable [15] for free surfaces. Other capillary force models may be implemented in this context.

In Sec. 2 of this paper we present the heat transfer, phase change and capillary flow

models. In Sec. 3 we present implementation of these models to the ISPH method. In this section we introduce our boundary condition model for heat transfer across the free surface. We also separately validate the heat transfer across free surface and melting across the free surface for different latent heat values in 2D and 3D. In Sec. 4 we present applications of this method to representative problems in additive manufacturing. We present the simulations of melting of complex shaped particles, compare the melting rate with available theoretical results for spherical shape to appreciate the effect of shape the ensuing viscous flow is coupled to the heat transfer problem. Finally, we simulate the agglomeration of a chain of three solid spheres undergoing melting with two different sets of material properties to show the shape evolution is a result of instabilities relating to the solid liquid interaction during the melting process.

2. Governing Equations

In the present study we assume the fluid (melt) and the solid to be incompressible, with negligible density variation during the phase change. The transient heat transfer in the system is governed by the enthalpy equation,

$$\frac{\partial H}{\partial t} = \nabla \cdot (k \nabla T), \quad (1)$$

where H is the enthalpy, k is the conductivity of the material and T the temperature. For an incompressible medium, the enthalpy H can be written as a function of temperature. Therefore,

$$\frac{dH}{dT} \frac{\partial T}{\partial t} = \nabla \cdot (k \nabla T). \quad (2)$$

Here dH/dT is the specific heat capacity at constant pressure, C .

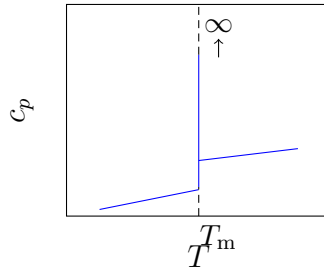


Figure 1: Increase of the specific heat capacity during the melting process.

Phase change (melting and solidification) can be modelled using the above equation by defining an effective heat capacity [2] which increases (or decreases) by the latent heat of

melting (or solidification), L , of the material at a melting (or solidifying) interface. This effective specific heat capacity can be defined as

$$C_{\text{eff}} = \begin{cases} C_s & T < T_m \\ C_m + L\delta(T - T_m) & T = T_m \\ C_l & T > T_m \end{cases} \quad (3)$$

where $\delta(T - T_m)$ is the Dirac delta function, C_s and C_l are the specific heat capacities of the material in the solid and liquid phases, respectively, and C_m is the specific heat capacity of the material at the melting interface, at the melting temperature. This model visually represented in Fig. 1. The specific heat capacity, in general, varies with temperature.

The liquid domain resulting from the melt is modelled here using a one-fluid formulation, neglecting the presence of air and is governed by the incompressible Navier Stokes equation given by:

$$\frac{d\mathbf{u}}{dt} = -\frac{1}{\rho}\nabla P + \nabla \cdot \left(\frac{\mu}{\rho}\nabla\mathbf{u} \right) + \mathbf{f}^{\text{int}} + \mathbf{f}^{\text{B}}. \quad (4)$$

Here P is the pressure, μ is the coefficient of viscosity, \mathbf{f}^{int} is the interfacial force acting at the free surface and at the liquid–solid interface and \mathbf{f}^{B} is the body force per unit mass acting on the system. The solid that undergoes melting is assumed to be rigid and interacts with the liquid domain through stresses at the interface.

The hydrodynamic pressure is $P = p + \tilde{p}$, where \tilde{p} is a background or ambient constant pressure which does not contribute to the pressure gradient force due to incompressibility of the medium. The pressure p is not coupled to the density and serves to ensure an incompressibility constraint such as a zero divergence velocity field

$$\nabla \cdot \mathbf{u} = 0, \quad (5)$$

or equivalently, an isochoric deformation given by a unit determinant of the deformation gradient tensor \mathbf{F} [17]

$$\det(\mathbf{F}) = 1. \quad (6)$$

The free surface of the fluid and its intersection with a solid surface (called the contact line) are subject to capillary forces modelled as inter particle forces. The numerical implementation of models for heat transfer, phase change, capillary fluid flow and the solid-fluid interaction based on Smoothed Particle Hydrodynamics is explained henceforth.

3. SPH implementation and validation

The SPH method is based on discrete computational nodes that carry field variable values and interact with each other within a cut-off radius associated with each node. A

smoothing function, W (also known as the kernel) and its derivatives are used to define continuous approximations of the field and its derivatives through convolution. Conservation of momentum is satisfied in the bulk through interparticle forces obtained through the kernel approximations.

For an incompressible fluid, the SPH formulation for momentum conservation is [22]:

$$\begin{aligned} \left. \frac{d\mathbf{u}}{dt} \right|_a = & - \sum_b m_b \frac{p_a + p_b}{\rho_a \rho_b} \nabla_a W_{ab} \\ & + \sum_b m_b \frac{\mu_a + \mu_b}{\rho_a \rho_b} F_{ab} \mathbf{u}_{ab} + \mathbf{f}_a^{\text{int}} + \mathbf{f}_a^B, \end{aligned} \quad (7)$$

where m is the mass, ρ is the density, p is the hydrodynamic pressure, μ is the coefficient of viscosity and \mathbf{u} is the velocity at a particle a or particle b in the neighborhood of a . Since \tilde{p} is a background pressure our implementation assumes $\nabla P = \nabla p$. The function W is a radially symmetric and positive definite smoothing function (also known as the smoothing kernel) with a finite cut off radius for the SPH discretization defined for a particle pair as $W_{ab} = W(r_{ab}, h)$, where h is the smoothing length of the kernel. The gradient of the smoothing function appears in the gradient terms as $\nabla_a W_{ab}$ for a particle a with respect to its neighbor b . The radial derivative of the kernel, given by F_{ab} [13] is computed from the gradient of W as

$$F_{ab} = \frac{\mathbf{r}_{ab} \cdot \nabla_a W_{ab}}{r_{ab}^2 + \epsilon^2} \quad (8)$$

where ϵ is a small number introduced to avoid division by zero in the rare event of particles overlapping in position and is usually set to $(0.01h)^2$.

The hydrodynamic pressure p in incompressible flows is nothing but a Lagrange multiplier that satisfies a constraint for incompressibility given by Eq. 5 or 6. For a divergence free velocity field, following grid based fluid simulation methods, pressure is obtained by solving the following pressure Poisson equation:

$$\nabla \cdot \left(\frac{1}{\rho} \nabla p \right) = \frac{\nabla \cdot \mathbf{u}}{dt}. \quad (9)$$

In the discrete SPH domain, the above equation can be approximated as

$$\sum_b \frac{m_b}{\rho_b} \frac{4(p_a - p_b)}{\rho_a + \rho_b} F_{ab} = \sum_b \frac{m_b}{\rho_b} \frac{\mathbf{u}_{ab} \cdot \nabla_a W_{ab}}{\Delta t}. \quad (10)$$

This approximation with unknown pressure values, represents a simultaneous system of linear equations in the unknowns p_a , and can be solved numerically using a linear solver such as

BiCGSTAB [20]. For a domain at least partly bounded by free surfaces, a Dirichlet BC for pressure can be semi-analytically applied by the following modification to this linear system [16]:

$$(p_a - p_o)\kappa - \sum_b \frac{m_b}{\rho_b} \frac{4p_b}{\rho_a + \rho_b} F_{ab} = \sum_b \frac{m_b}{\rho_b} \left(\frac{\mathbf{u}_{ab} \cdot \nabla_a W_{ab}}{\Delta t} - \frac{4p_o}{\rho_a + \rho_b} F_{ab} \right) \quad (11)$$

where p_o represents the ambient pressure and κ , given by

$$\kappa = \sum_{b_{\text{bulk}}} \frac{m_b}{\rho_b} \frac{4}{\rho_a + \rho_b} \frac{\mathbf{r}_{ab} \cdot \nabla_a W_{ab}}{r_{ab}^2 + \epsilon^2}, \quad (12)$$

is a factor which remains constant for a given domain with given smoothing parameters and constant density. This modification effectively applies a penalty term that accounts for the deficiency of the kernel for a particle near the free surface, and does not add to the computational cost.

Capillary forces are modelled using an inter-particle force function $\mathbf{f}_{ab}^{\text{int}}$ based on the molecular theory of surface tension [19, 23] and is chosen to have an attractive part in the long range and a repulsive part in the short range. This capillary model is elaborated in a recent publication in the context of dynamic free surface flows [15]. We use the following pairwise force:

$$F_{\alpha\beta}^{\text{int}}(r_{ab}) = \begin{cases} -s_{\alpha\beta} \cos\left(\frac{3\pi}{4}q_{ab}\right) & q_{ab} = \frac{r_{ab}}{h'} \leq q_{\text{cutoff}} \\ 0 & q_{ab} = \frac{r_{ab}}{h'} > q_{\text{cutoff}}, \end{cases} \quad (13)$$

where α and β represent the phases of the particles a and b , respectively. The strength of the pairwise force is given by $s_{\alpha\beta}$. Here the cut off distance of the pairwise force is set to be the same as that of the smoothing kernel. The strength of the pairwise force for a given macroscopic surface tension can be predetermined [23] in the presence of a free surface and this relationship is [15]:

$$\sigma = \lambda s_{ll} h_r^4, \quad \text{for 2D and} \quad (14)$$

$$\sigma = \lambda s_{ll} \frac{h_r^5}{\Delta x} \quad \text{for 3D,} \quad (15)$$

respectively. Here, h_r is the ratio of the smoothing length of the kernel to the initial particle spacing Δx (here we use a square lattice arrangement of particles as the initial condition). Note that these expressions correspond to the specific choice of pairwise force function and compact support. The constant due to integration of the pairwise force function, λ takes the value 0.0476 in two dimensions and 0.0135π in three dimensions, respectively, for the interaction function given by eq. 13. We use an explicit viscous force approximation (the second term on the right hand side) that is extensively used in SPH literature [14] especially for low Reynolds number flows.

3.1. Heat transfer across free surface

Heat transfer problems have been solved in SPH using the approximation of second order derivatives. In finite domains, the kernel of SPH gets truncated at the interface. Our intended applications require ambient boundary conditions. This is achieved by a semi analytic Dirichlet BC for temperature similar to the application of Dirichlet pressure BC in the Laplacian of pressure presented in the previous section.

The heat transfer model (Eq. 2) is approximated in the SPH domain as follows:

$$C\rho\frac{dT}{dt} = \sum_b \frac{m_b}{\rho_b} \frac{4}{\rho_a + \rho_b} F_{ab} \left(\frac{k_a + k_b}{2} T_{ab} \right) \quad (16)$$

where, k_a and k_b represent the conductivity at the node a and b respectively and $T_{ab} = T_a - T_b$.

Following a similar approach to the free surface Dirichlet BC for the pressure Poisson equation [16] presented above in Eq. 11, Dirichlet boundary condition for temperature can be applied semi-analytically, as well. Applying this to the eq. 2 would lead to the following heat transfer equation approximation:

$$C\rho\frac{\partial T}{\partial t}\bigg|_a = \sum_b m_b 2 \frac{k_a + k_b}{\rho_a + \rho_b} F_{ab} (T_a - T_b) + \kappa \frac{k_a + k^o}{2} \rho_a (T_a - T^o), \quad (17)$$

where κ is the same constant as in Eq. 12 and T^o is the ambient temperature (which can be time varying).

The accuracy of heat transfer is central to our problem and requires careful validation. For this, we solve the 2D heat conduction problem for a flat plate with free surfaces on all sides and with an adiabatic wall on one side. The adiabatic wall is modeled using static particles.

The heat conduction through the flat plate across the free surface is compared to the analytical solution at different times in Fig. 2 where the plate is heated at constant temperature from the ambience on all four sides. An array of 80×80 fixed particles are used to represent a square flat plate of side 0.1 m. The ambient temperature is set to 0 K and the plate is set to a uniform initial temperature of 1 K. The density of the material is set to 1 kgm^{-3} and the thermal diffusivity is set to $1 \times 10^{-4} \text{ m}^2\text{s}^{-1}$.

In Fig. 3, one of the walls of the plate is set to be adiabatic wall where a homogeneous Neumann BC is applied for temperature by setting zero temperature gradient between particles of the domain and the adiabatic wall. The solutions are compared to analytical solutions, available widely in standard text books on numerical methods [9], and a very good match is observed.

The consistency of this heat transfer model can be seen in Fig. 4, showing greater than first order accurate. The L_2 norm of the error at different times are presented against the

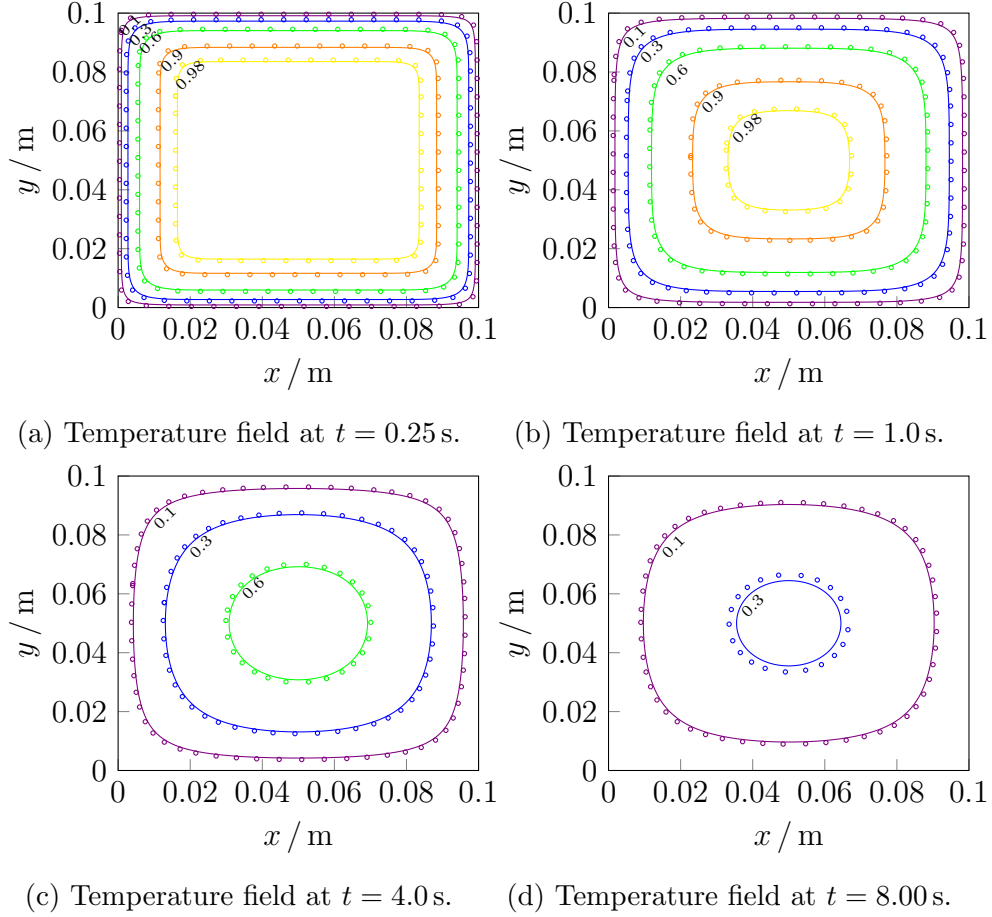


Figure 2: Evolution of temperature profile within a square at different times for a resolution of 160×160 particles with Dirichlet BC on all sides.

resolution of the domain. The order of accuracy of the heat transfer simulation with the free surface BC can be clearly seen to be more than first order in Fig. 4.

3.2. Static phase change

Phase change is modelled using the effective heat capacity C defined in Eq. 3. There are different strategies for implementing the effect of latent heat into a numerical method. On the one hand it can be added as a source term to the heat conduction equation [26, 18] or, on the other hand, by modifying the heat capacity itself [2, 24, 5]. In this work an integral interpolation introduced by [2] is implemented to modify the heat capacity in order to model phase change processes because of its low computational costs. Therefore, the

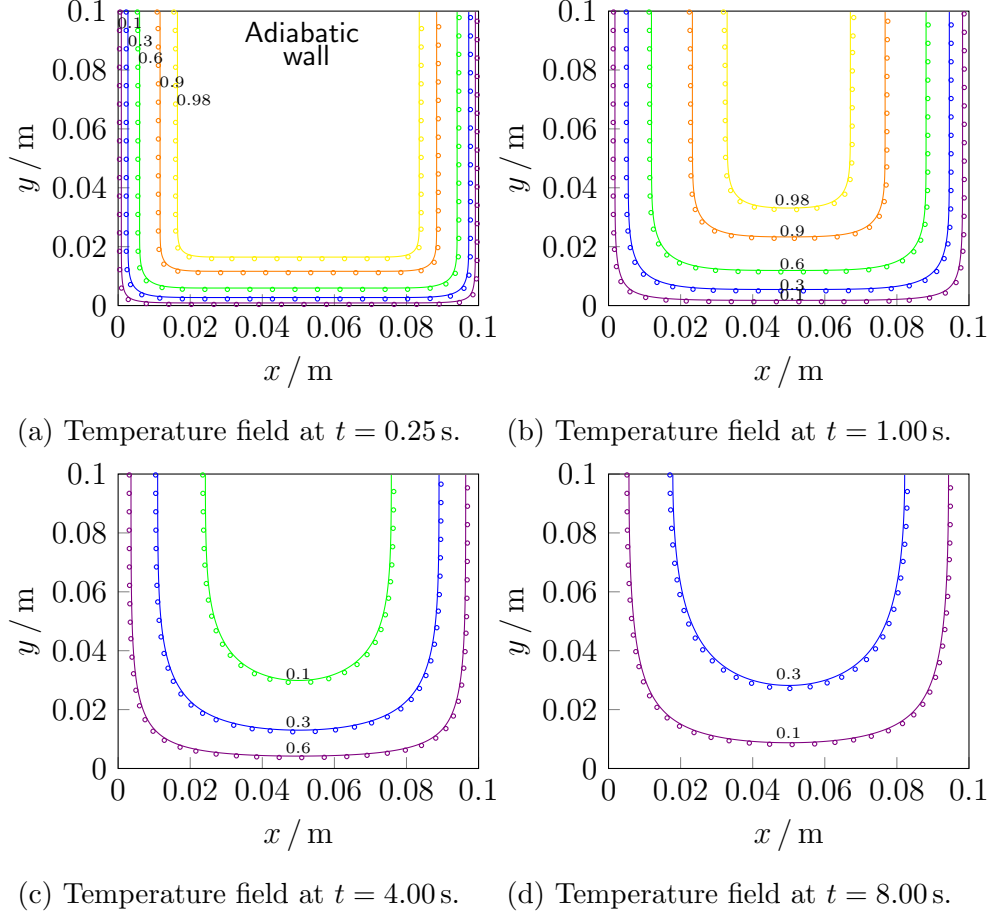
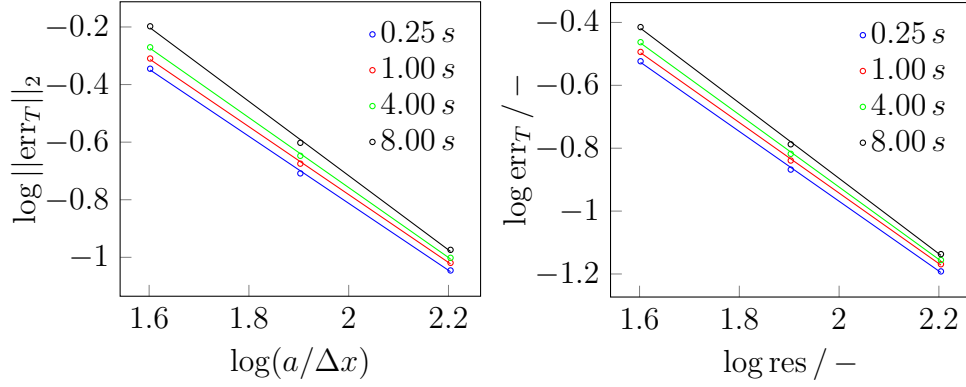


Figure 3: Evolution of temperature profile within a square at different times for a resolution of 160×160 particles with Dirichlet BC on three sides and Neumann on the fourth.

model for a smoothed latent heat in SPH can be derived by starting from the definition of an effective heat capacity C_{eff} which includes the effect of latent heat [1, 6] given by Eq. 3. This formulation is composed of the heat capacities for solid C_s and C_l liquid phase as well as the heat capacity within the phase change region C_m . Here, C_{eff} at the melting temperature T_m includes the total latent heat of the phase change, $L = \int_{-\infty}^{\infty} L \delta(T - T_m)$.

The Dirac function can be replaced in the one-dimensional temperature domain by a kernel function W_T with smoothing length h_T analogous to the spatial kernel function in



(a) Dirichlet BC on all sides

(b) Dirichlet BC on three sides and homogenous Neumann BC on one.

Figure 4: L_2 norm of the error in temperature (T) in the domain at different times for different spatial resolution. The plot shows the order of accuracy is greater than 1 at all time instances.

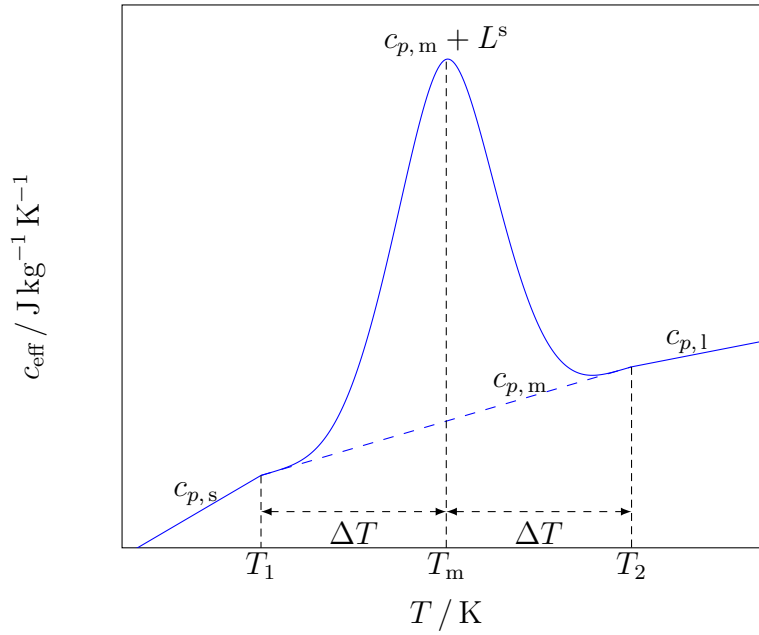
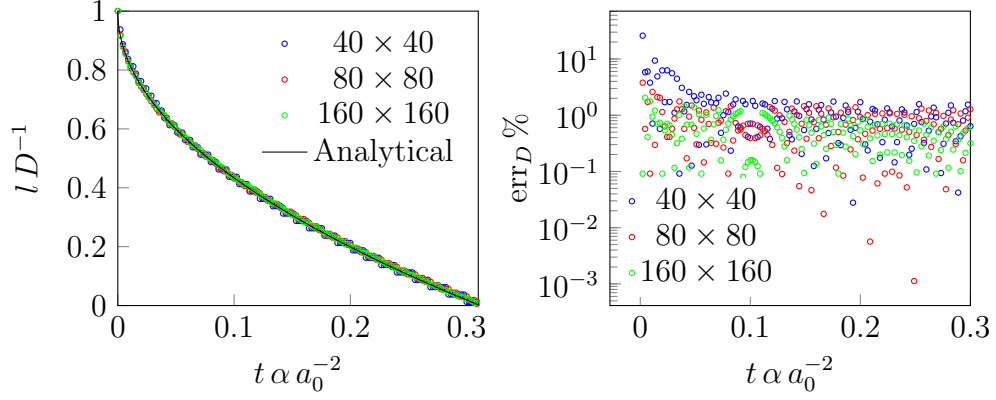


Figure 5: Smoothed effective heat capacity within the mushy region of the phase transition temperature.

SPH resulting in:

$$C_{\text{eff}} = \begin{cases} C_s & T < T_m - \Delta T \\ C_m + LW_T(T - T_m, h_T) & T_m - \Delta T \leq T \leq T_m + \Delta T \\ C_l & T > T_m + \Delta T \end{cases} \quad (18)$$



(a) Dimensionless interface position along diagonal vs dimensionless time. (b) Error in interface position

Figure 6: Stefan's problem: Interface position (a) and calculated errors (b) obtained for different resolutions.

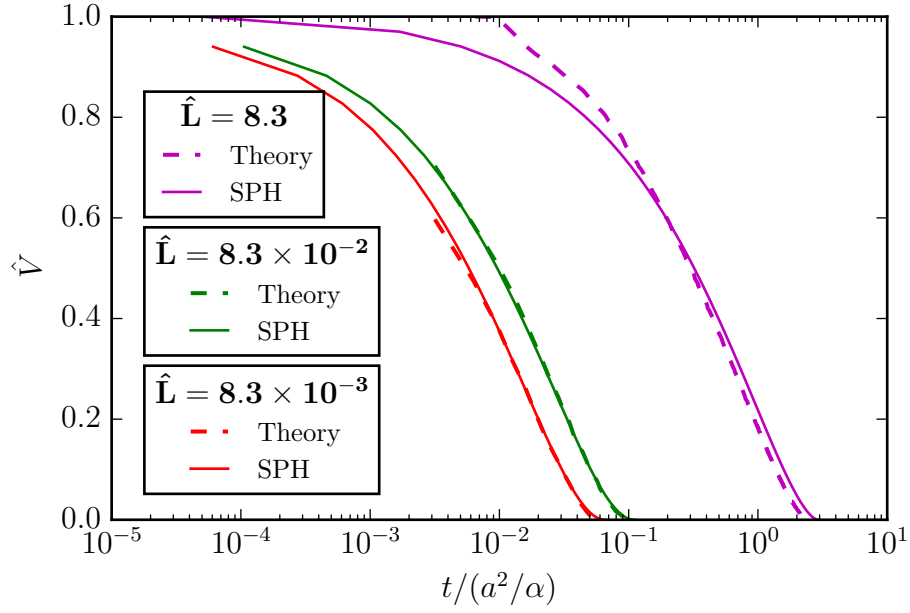


Figure 7: Static melting of a spherical solid—comparison of evolution of solid volume fraction with 1-D axisymmetric theory

The temperature domain ΔT represents a mushy region around the phase change temperature. The size of this region is defined as the product of the smoothing length h_T and the maximum range of support q_{\max} of the temperature kernel.

$$\Delta T = h_T q_{\max}. \quad (19)$$

The outcome of this is a changing C_{eff} inside of this region with a maximum latent heat effect at the transition temperature. The accuracy of this approach is further improved by considering the distance between adjacent particles and the temperature difference with respect to the transition temperature. This results in a smoothed latent heat L^s [2] for a particle a defined as

$$L_a^s = \sum_b \frac{m_b}{\rho_b} (L W_T(T_b - T_m, h_T)) W(\mathbf{r}_b - \mathbf{r}_a, h). \quad (20)$$

This results in the effective heat capacity given in equation (21) which is replacing the specific heat capacity of the heat conduction equation (16).

$$C_{\text{eff}} = \begin{cases} C_s & T < T_m - \Delta T \\ C_m + L^s & T_m - \Delta T \leq T \leq T_m + \Delta T \\ C_l & T > T_m + \Delta T \end{cases} \quad (21)$$

The apparent heat capacity with a smoothed jump for the latent heat is shown in Fig. 5.

The phase change model in SPH together with the free surface BC for ambient temperature needs to be validated. Here we choose the classical Stefan's problem in 2D and an axisymmetric version in 3D to validate the evolution of the melting interface with time.

In two dimensions, the two edges of a right angled corner of a 2D square plate is heated. The medium is set to a density of 1 kg/m^3 . The initial and melting temperature are set to 2 and 2.3 K respectively. The conductivity and specific heat capacity of both phases were maintained at a value of 1 in SI units. The latent heat capacity was set to 0.25 J/kg . Three different resolutions were considered corresponding to 40, 80 and 160 particles along one direction in the quarter space of dimensions $a = 3 \text{ m}$. The choice of these parameters are arbitrary, since the aim of the validation is only to check the numerical approximation of the model. In the following section we will resort to more realistic simulation parameters. As the temperature rises above the melting temperature, the solid melts and the solid liquid interface moves inwards. The location of the phase change interface along the diagonal, normalized by the width of the plate is plotted against non-dimensional time in Fig. 6a. The melting process is assumed to be static, such that the molten region is assumed to not

deform. This problem is simulated, without liquid deformation for different spatial resolution and compared against the analytical solution. Note that the heat transfer across the free boundary is based on the semi-analytic boundary formulation in Eq. 11. The interface location appears as a stepped curve because of the discrete sampling in time. We see that the interface evolution is predicted accurately. In Fig. 6b we see the order of accuracy increase with increasing resolution, consistently. The discrete sampling in time makes it difficult to obtain the exact order of accuracy.

In three dimensions, we solve the Stefan's problem in a sphere and compare the results with the solutions of a one dimensional axisymmetric model proposed in [12], given by

$$\frac{\partial h}{\partial t} = \frac{\partial^2 \hat{T}}{\partial r^2} + \frac{2}{r} \frac{\partial \hat{T}}{\partial r} \quad \text{in } 0 < r < 1, \quad (22)$$

where r is the radial location in the unit sphere, normalized by the radius of the sphere, R . Time is normalized by R^2/k_s , where k_s is the conductivity of the solid phase. The enthalpy h is related to the temperature \hat{T} (normalized by $\Delta t = T_a - T_m$) by

$$T = \begin{cases} h - \beta, & h < 0 \\ 0, & 0 \leq h \leq \beta, \\ \tilde{k}(h - \beta), & h > \beta, \end{cases} \quad (23)$$

where β , the Stefan number is given $\beta = L/(c\Delta T)$, where c_s is the specific heat capacity of the solid phase. Also \tilde{k} represents the ratio of thermal diffusivities of the solid and liquid phases respectively, $\tilde{k} = k_l/k_s$. Eq. 22 is solved using finite difference method as given in [12] and [25]. We discretized the spatial derivatives using a central difference approximation and the temporal derivatives using forward time Euler approximation and solved the system explicitly to obtain the melting interface position in time.

In order to motivate application to realistic materials, we present the results for different latent heat capacities spanning different orders of magnitude. Though the results presented are non-dimensionalized, the material parameters are chosen to resemble realistic materials and these parameters will be used for further simulations in the dynamic context in the next section. In Fig. 7 we present the time evolution of melting. Instead of the location of the interface position, we present the volume of the solid remaining at different instances in time. Since our goal is to present the effect of shape of the melting body, we choose the volume of the solid instead of a linear dimension. The simulation and discretization parameters are presented in Table 1. Three different latent heat values are considered.

We see that for lower latent heat values, the match is accurate, however for large latent heat values, the onset of melting is slightly different from the analytic solution. This is perhaps due to the truncated temperature and spatial kernel used in computing the latent heat. We will be addressing this in a future work.

Quantinty	Value	Unit
σ	0.2308	Nm ⁻¹
Θ	30	°
η	0.001793	Pa s
ρ	1000	kg m ⁻³
T_0	1	K
T_m	1.15	K
T_{amb}	4.0	K
C	2110.0	J kg ⁻¹ K ⁻¹
L	0.1, 1.0, 100.0	kJ kg ⁻¹
k	2.14	W m ⁻¹ K ⁻¹
Δx	4.0×10^{-5}	m
ΔT	0.1	K
R	5.66×10^{-4}	m

Table 1: Parameters used to simulate melting of a sphere and a milled particle.

The time update is numerically stable only when Δt satisfies the condition

$$\Delta t \leq \min_a \left(0.25 \frac{h}{3|\mathbf{u}_a|}, 0.25 \sqrt{\frac{m_a h}{3|\mathbf{f}_a^{\text{int}}|}}, 0.25 \frac{\rho h^2}{9\mu} \right). \quad (24)$$

4. Applications: Melting dynamics

The multiphysics SPH algorithm is implemented in an ISPH code [16, 17] and melting problems with flow dynamics are solved for complex shaped three dimensional solids. Results are compared with theoretical results and other studies with simpler assumptions.

4.1. Melting of a mill particle

A complex shaped geometry obtained by scanning a milled particle from an industrial process is shown in Fig. 8. This geometry is filled with SPH particles in a square array with the same intial spacing and simulation parameters as that is used in the validations using melting of a sphere presented in the previous section. Even the volume of the sphere in the previous section was chosen to be equal to the volume of the mill particle. We have avoided discontinuities in the thermal properties across the solid liquid interface in order to compare with the theoretical results and to focus on the melting and capillary force based

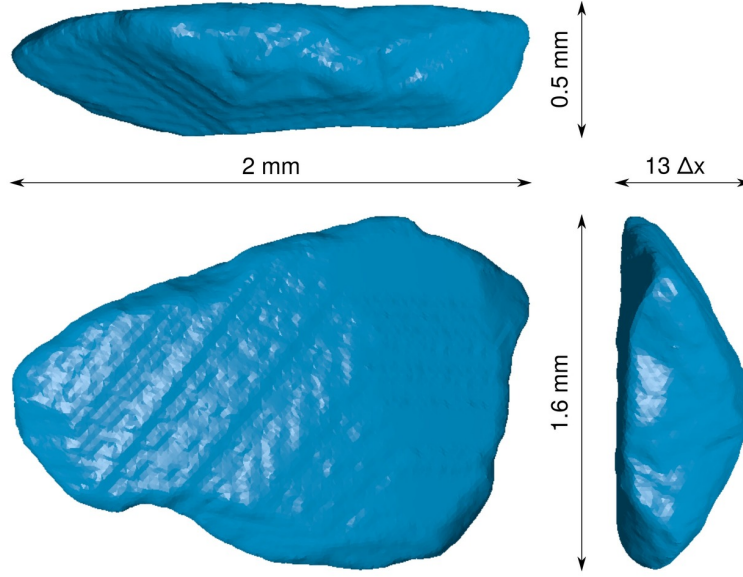


Figure 8: Complex shaped mill particle: dimensions in mm and in initial SPH particle spacing.

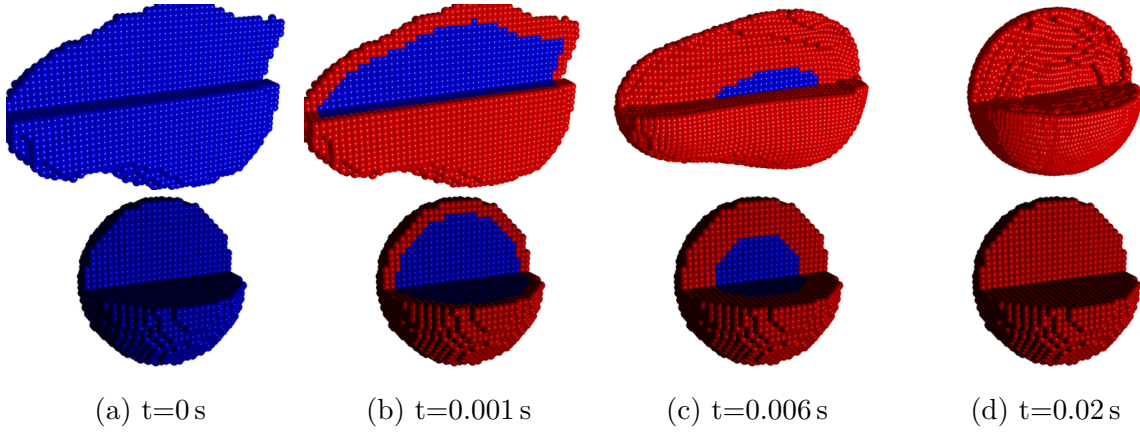


Figure 9: $L = 0.01 \text{ kJ/kg}$: Melting of an irregular shaped mill particle vs a static sphere. Blue colored particles denote solid and red colored particles liquid state.

deformation as the first step. Discontinuities in this regard will be introduced in the next section.

The evolution of the solid and liquid phases are shown in Fig. 9–14. Since different phys-

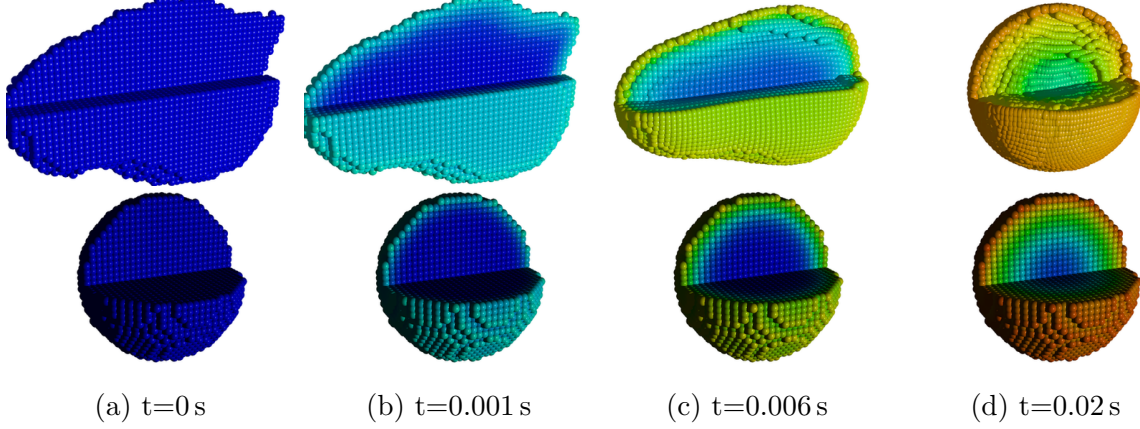


Figure 10: $L = 0.01\text{ kJ/kg}$: Temperature distribution in the melting mill particle.

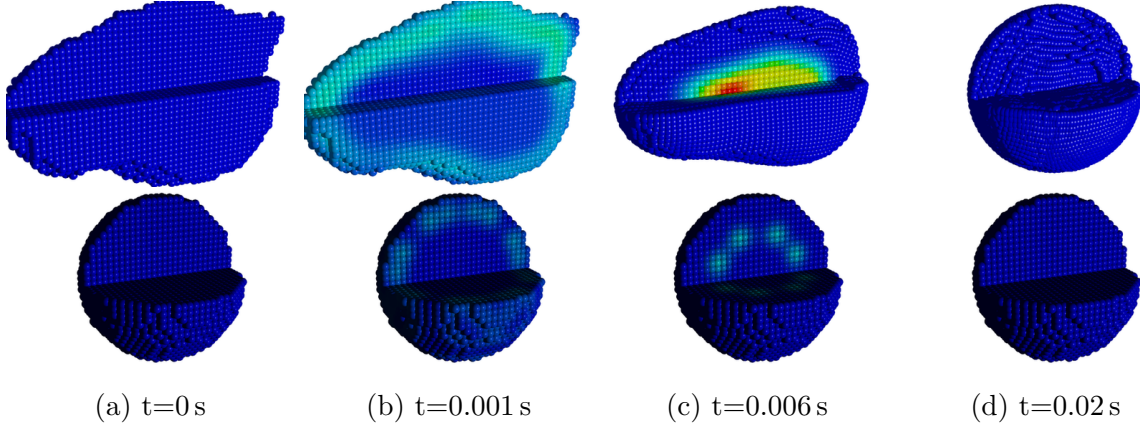


Figure 11: $L = 0.01\text{ kJ/kg}$: Latent heat absorbed at the interface during the melting of the mill particle.

ical processes are coupled in this simulation, we have not attempted to non-dimensionalize this system. However the rate of phase change is non dimensionalized and compared with the melting of the sphere in the earlier section.

In Figs. 9 and 12 blue and red particles represent solid and liquid phases, respectively. For better illustration, a quadrant is clipped out of the irregular particle to show the interface evolution in the bulk of the particle. At the beginning of the simulation, all SPH particles are in solid state. As a result of the heat exchange with the ambience, the phase change occurs as a particle temperature rises above the melting point. A layer with liquid SPH particles are formed on top of the surface of the irregular shaped particle after about 0.001 s .

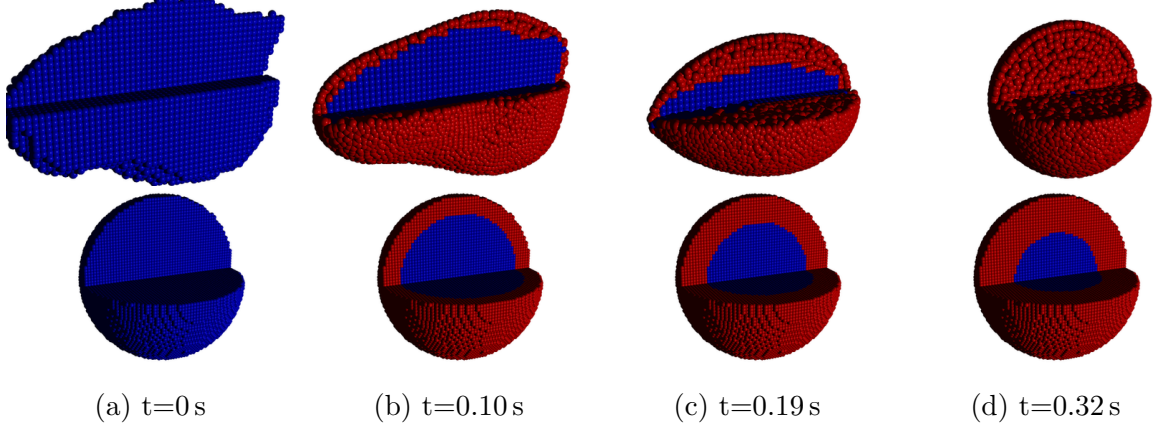


Figure 12: $L = 100.0 \text{ kJ/kg}$: Melting of an irregular shaped mill particle vs a static sphere. Blue colored particles denote solid and red colored particles liquid state.

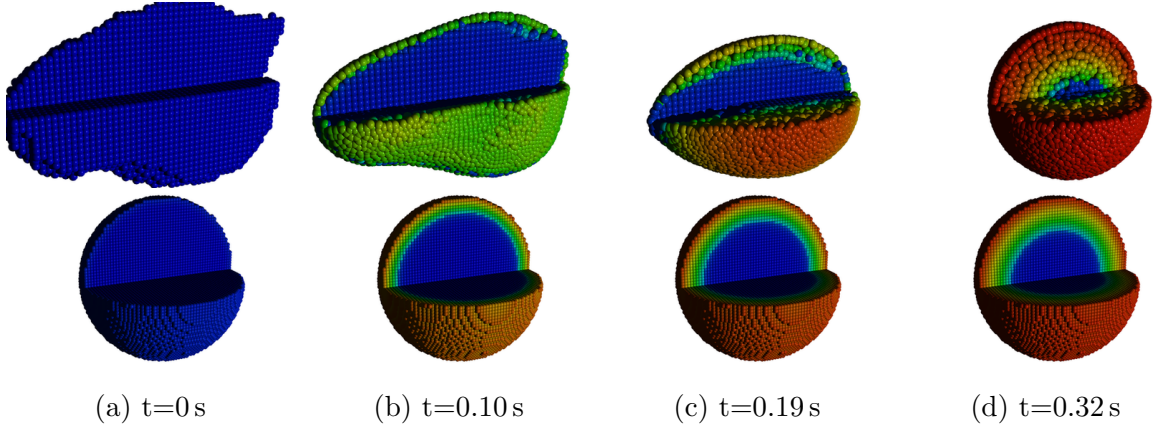


Figure 13: $L = 100.0 \text{ kJ/kg}$: Temperature field in the melting particles. Top row shows the mill particle with flow of melt and the bottom row shows a static spherical particle.

The liquid solid interface is hydrophilic owing to the acute contact angle of 30° , resulting in a wetted surface. The flow of the liquid due to capillary forces influences the heat exchange due to the evolving geometry.

Shortly after a thin layer is melted, the shape of the body smoothes out by 0.005 s . We have presented the simulation until all the solid is finally melted. After the solid is completely melted, the resulting liquid drop performs oscillations until relaxation to a spherical shape of minimum surface area.

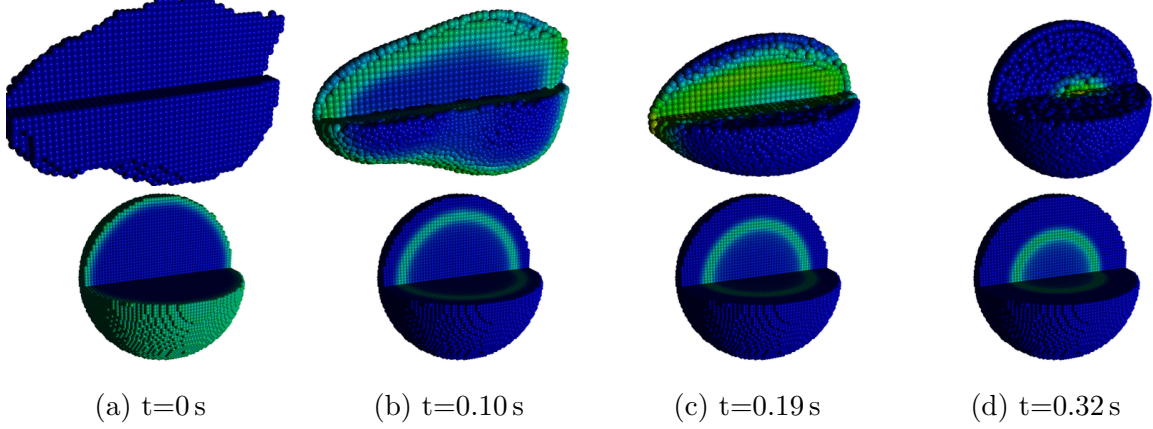


Figure 14: $L = 100.0\text{ kJ/kg}$; Latent heat absorbed at the interface during the melting of the mill particle.

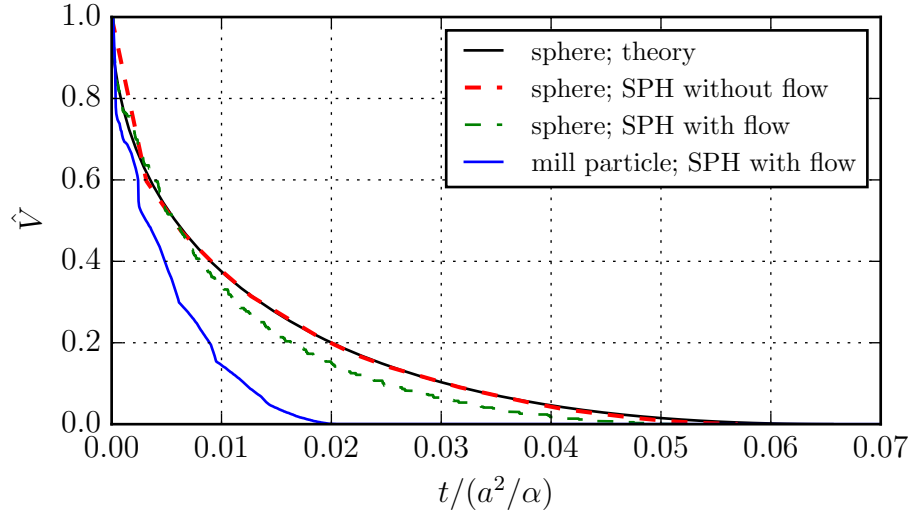


Figure 15: Time variation of volume fraction of solid for a sphere and the mill particle of equal volume.

In Figs. 10 and 13, the temperature field of the melting body is shown. With the onset of heat exchange with the ambiance the initial solid particles start to heat up. At 0.001 s the particles have the same temperature depending on the exposure to free surface. Due to the convective movement of the particles caused by surface tension, liquid particles are moving to the vicinity of the solid body, where they cool down. It is also possible that colder liquid

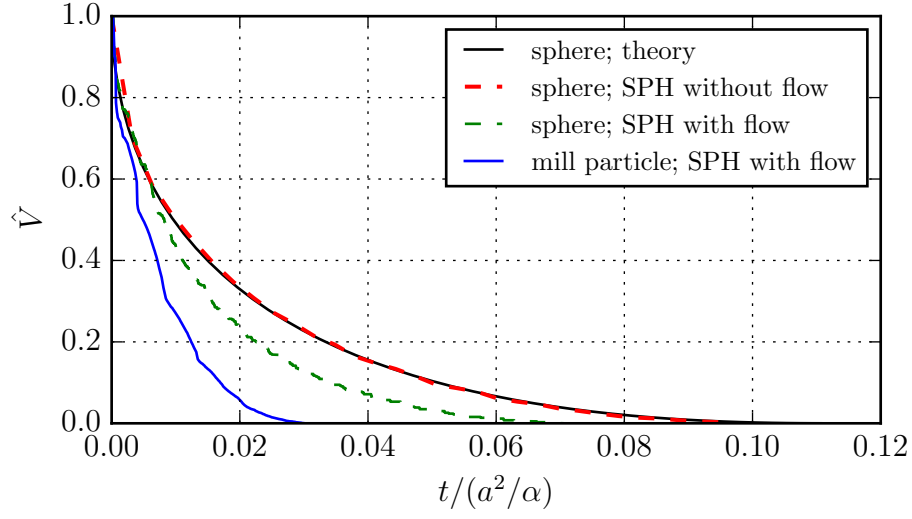


Figure 16: Time variation of volume fraction of solid for a sphere and the mill particle of equal volume.

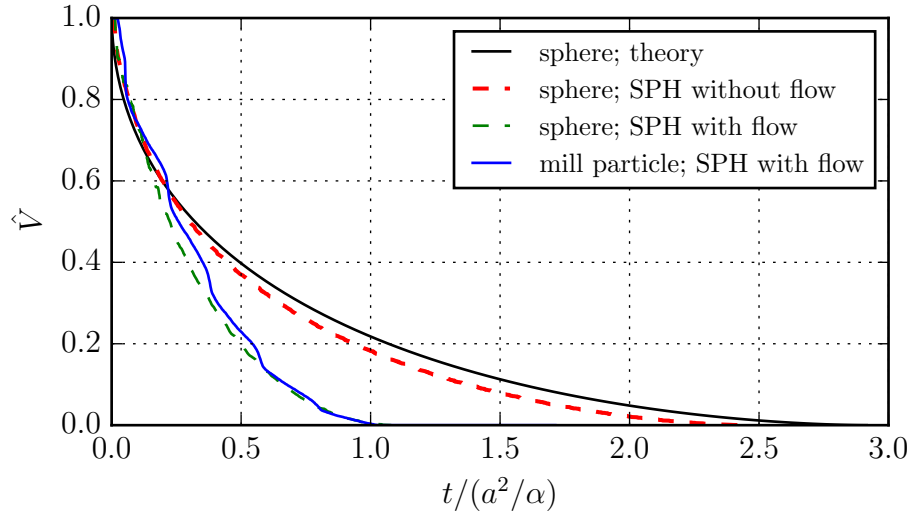


Figure 17: Time variation of volume fraction of solid for a sphere and the mill particle of equal volume.

particles are transported back to the surface where they are warmed up. This results in an irregular distribution of particles with different temperatures at a certain time which can already be seen after 0.013 s and is further strengthened during the melting process until all particles are completely in liquid state.

In Figs. 11 and 14, the area of effect of the normalized latent heat is shown. As the temperature rises, particles enter the mushy region where the effect of latent heat increases. Red colored particles characterize a high effect of latent heat and blue colored particles characterize particles that are not influenced by the latent heat. It can be seen that the edges of the irregular shaped particle are first influenced by the phase change. Since the still unfused rigid body moves to the upper edge of the particle, the effect of the latent heat remains exclusively on the upper hemisphere of the sphere formed around the solid body.

The same simulation with properties given in Table 1 was performed for a latent heat of $L = 100 \text{ kJ/kg}$. The process of phase change is shown in Fig. 9. In this case, the phase change happens slower than the movement of liquid particles due to surface tension. It takes 0.40 s until all solid particles are melted. In comparison to a latent heat of $L = 1 \text{ kJ/kg}$ with a melting time 0.037 s this is approximately ten times slower. It can be seen that the liquid particles are moving behind the rigid body at $t = 0.15 \text{ s}$ where they are forming a sphere. One reason for this could be an unequal melting rate on both sides of the solid body. Therefore, the liquid particles are moving to the side with more liquid particles at a specific time. Another reason could be the infiltration of the liquid particles through the rigid body, which is a numerical issue. In comparison to the previous case with $L = 1 \text{ kJ/kg}$ the rotation of the rigid body within the forming liquid sphere is increased as shown in the time interval 0.15 s to 0.25 s. This effect results from the fact that the solid particles are melting more slowly. That is why the exchange of forces between liquid particles and rigid body is not altered by the phase change process as much as for a lower latent heat number. As the rigid body shrinks it is moving towards the liquid spheres center which is in contrast to the case for the latent heat of $L = 1 \text{ kJ/kg}$ as shown in Fig. 12.

In Fig. 13 the temperature distribution for each investigated time is shown. At the beginning, the irregular shaped particle has a uniform initial temperature of 1.00 K. As the time proceeds, the temperature rises at the solid bodies surface. Due to the latent heat there is a high temperature gradient between solid and liquid particles as it can be seen at $t = 0.15 \text{ s}$. After $t = 0.40 \text{ s}$ the maximum temperature occupied by a liquid particle is 3.43 K and hence approximately 1 K above the highest temperature in the previous case with $L = 1.00 \text{ kJ}$. Because the time needed for melting increases with the latent heat, the liquid particles temperature tends to reach an equilibrium value as shown in the time interval between 0.3 s and 0.4 s.

The normalized latent heat for the irregular shaped particle with $L = 1 \text{ kJ/kg}$ can be seen in Fig. 14. One difference to Fig. 11 is the propagation of the areas where latent heat comes

into action which is caused by the rigid bodies position.

The evolution of solid fraction with time for all three latent heat values are show in Figs. 15, 16, 17. Here the analytical and static sphere results are the same as in Fig. 7. We have also included dynamic melting of spheres in these figures in order to detect increased heat transfer due flows due to instabilities. The increased heat transfer of a dynamic sphere suggests the presents of capillary flows, which exacerbates for larger latent heat values.

4.2. Agglomeration of a chain of melting solids

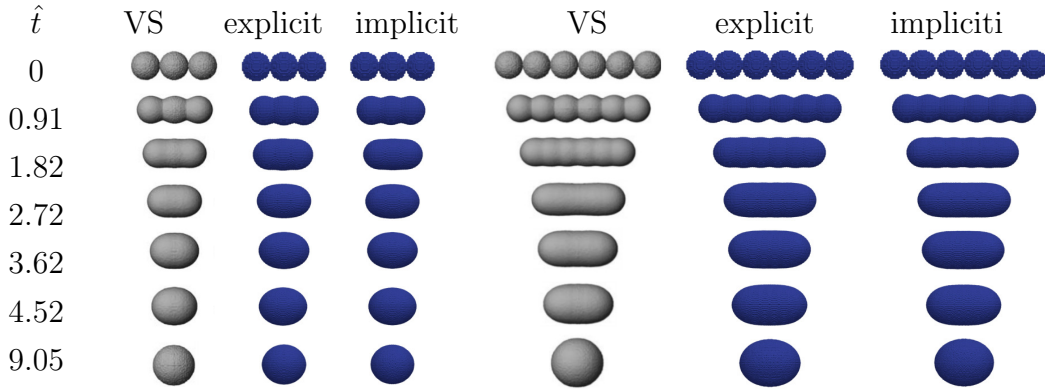


Figure 18: Shape evolution of agglomerate chains with three and six spheres. On the left side of each subfigure are the solutions by [7]. The centered column are the solutions with an explicit and the right side with an implicit method.

In order to motivate the application of the proposed SPH approach to understand structural evolution of melting solids with realistic transport and thermal properties, we present the simulation of agglomeration of melting spheres. Sintering is sometimes approximated as a slow viscous flow [7] in the low Reynold's number regime. In such an assumption, which is indeed valid for many engineering applications, a non dimensional time can be defined as [8]

$$\hat{t} = \frac{t\sigma}{\eta r_0}, \quad (25)$$

where σ is the surface tension, η is the dynamic viscosity, r_0 is the characteristic length and t , the time. However, when the melting dynamics and heat transfer is fully resolved, the resulting structural change cannot be represented by a single non dimensional quantity. In table 2. we present the transport and thermal properties of the materials we simulate. However, a high viscosity of 1Pa·s is used for the viscous flow sintering simulation. As mentioned before, the issue of even higher viscosity is outside the scope of the current paper and will be dealt with in a future work.

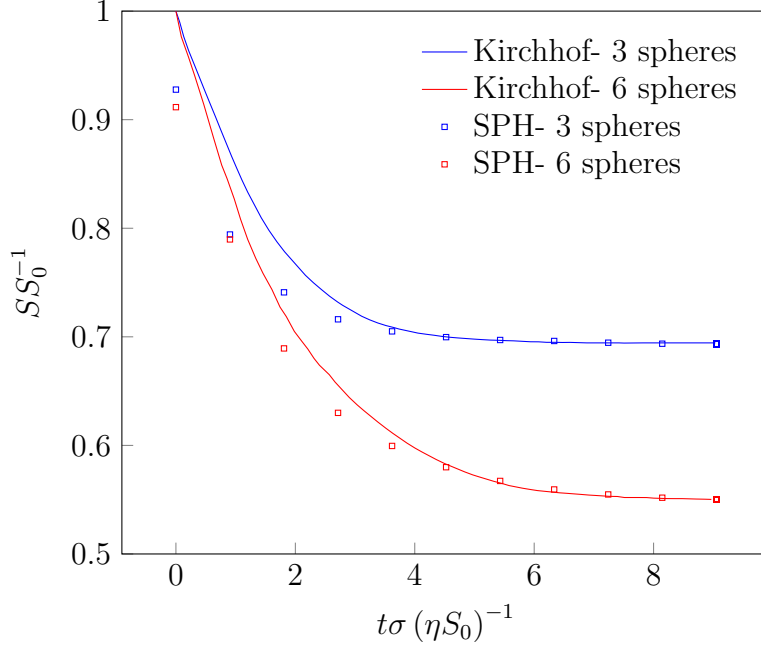


Figure 19: Dimensionless surface area evolution of agglomerate chains with three and six spheres. The surface area is normalized with the initial surface area S_0 of the primary particles. The normalized surface area determined by [7] are given as solid lines whereas the results from are shown as hollow circles.

Initially we perform simulation of viscous sintering similar to that given in [7]. In Fig. 18, we compare the viscous sintering results from [7] with SPH flow simulations. A very good visual agreement is observed. Further, in Fig. 19, the evolution of dimensionless surface area of the agglomerate spheres is confirmed and the quantitative agreement is seen.

We then present the melting dynamics of 3 spheres with finite latent heat value of 100 kJ/kg. The phase, temperature and local latent heat are presented in figures, 20, 21 and 22 respectively at different time instances. After 0.0025 s, a thin layer of liquid is formed on the spheres, which coalesce with the adjacent spheres. The resulting fluid-solid interaction results in complex free surface evolution, remarkably different from the assumption of viscous sintering. Also, as seen at the time instance of 0.1341 s, two out of the three primary spheres are molten completely, implying that the non linear motion of the spheres also affect heat transfer in the bulk of the material.

The shape evolution of dynamically melting agglomerate chain of spheres with different latent heat capacities is then compared against the viscous flow assumption. Note that the viscous flow simulations have a viscosity 1000 times larger than that of the melting

Table 2: Thermodynamic properties of the solid and liquid particles as well as the ambient pseudoparticles for the melting of an agglomerate chain with three primary spheres.

Quantity	Value	Unit
σ	$7.12 \cdot 10^{-2}$	N m^{-1}
Θ	30.00	$^{\circ}$
η	$1.00 \cdot 10^{-3}$	Pa s
ρ	$1.00 \cdot 10^3$	kg m^{-3}
T_0	1.00	K
T_m	1.15	K
k_s	2.14	$\text{W m}^{-1} \text{K}^{-1}$
k_l	0.56	$\text{W m}^{-1} \text{K}^{-1}$
$c_{p,s}$	$2.11 \cdot 10^3$	$\text{J kg}^{-1} \text{K}^{-1}$
$c_{p,l}$	$4.22 \cdot 10^3$	$\text{J kg}^{-1} \text{K}^{-1}$
L	1.00	J kg^{-1}
T_{amb}	4.00	K
k_{amb}	0.56	$\text{W m}^{-1} \text{K}^{-1}$
$c_{p,\text{amb}}$	$4.22 \cdot 10^3$	$\text{J kg}^{-1} \text{K}^{-1}$

simulation, while the latent heat of the melting spheres is 100 kJ/kg. At these values, the shapes evolved at comparable rates as seen in Fig.23. Since the fluid is not all molten for the given time instances, the fluid-solid interaction results in complex shapes, often resulting in low aspect ratio shapes compared to the result from the linear assumptions.

5. Conclusions

A multiphysics, coupled heat transfer, phase change and capillary flow solver is presented in the context of Incompressible Smoothed Particle Hydrodynamics. A constant volume melting model is implement. The model is based on a spefic heat that increases additively by the latent heat of the material, near the melting interface and at temperatures close to the melting point. Heat transfer accross the free surface through a semi analytic Dirichlet BC across the free surface allows the study of complex shaped bodies. The method is carefully validated against theoretical models on melting and conduction heat transfer.

The method is first applied to study the influence of particle shape on it surface evolution during heating and subsequent melting of the particle. We simulate melting process across a range of latent heat values and show that at high latent heat values the melting process evolves substantially differently from assumptions of a spherical shape. A non spherical

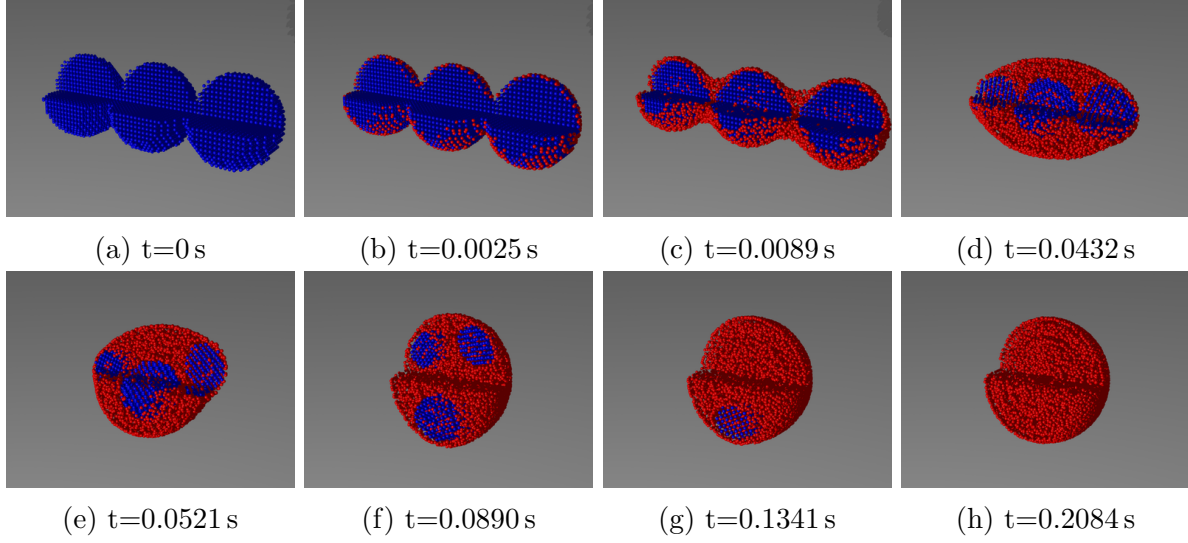


Figure 20: Representation of the solid-liquid phase change of an agglomerate chain with three primary particles. Blue colored particles denote solid and red colored particles liquid state. Melting occurs until all particles are in the liquid state and form a sphere.

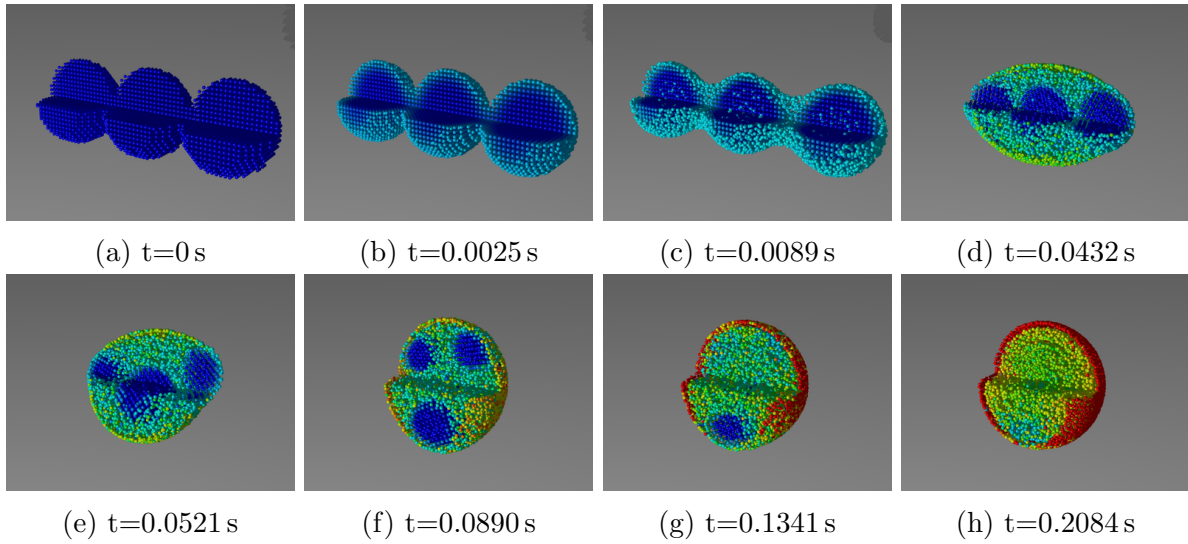


Figure 21: Temperature distribution of three primary particles forming an agglomerate chain and liquid state particles formed during the melting process. The temperature takes values between 1.0 K (blue colored) and 3.034 K (red colored).

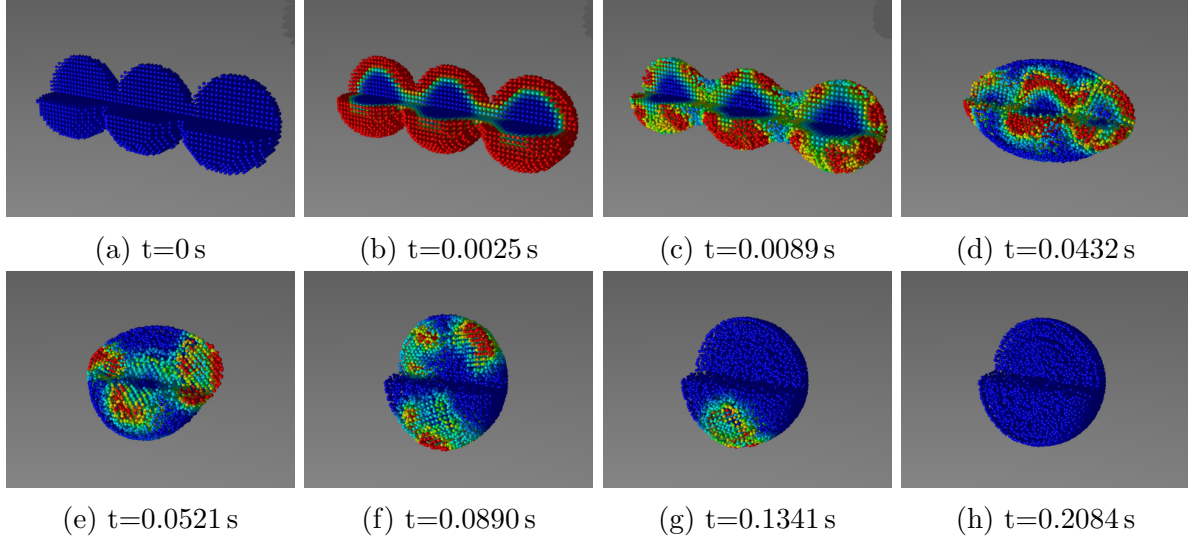


Figure 22: Representation of the regions in which the particles are located in the temperature range of the phase change. The effect of latent heat is normalized and has its greatest effect in red-colored areas. Blue colored particles are outside the mushy-region for the phase change and experience no effect due to the latent heat.

shape causes capillary flow of the melt, increasing heat transfer due to convection within the melt accelerating the melting process.

The method is then applied to the study of agglomeration of a chain of particles that undergo melting. The results are compared against simulations that assume viscous sintering. We show that when unmolten solid particles are present (owing to large latent heat of melting of the material), the evolution of shape of the agglomerate follows a highly non linear path due to the fluid-solid interaction within the body of the melt. Thus a case is made for the method's application to microstructure studies in additive manufacturing where time scales of the flow and phase change are comparable.

In this work, we have used representative transport and thermal properties. However this doesn't span the entire range of properties encountered in real applications. For example high viscosities encountered in additive manufacturing using polymers would require implicit computation of viscosities. Simulations with high latent heat require adaptive time stepping to reduce computational costs. These improvements in computational efficiency will enable simulations of large number of particles needed for relating microstructure to bulk properties of manufactures parts.

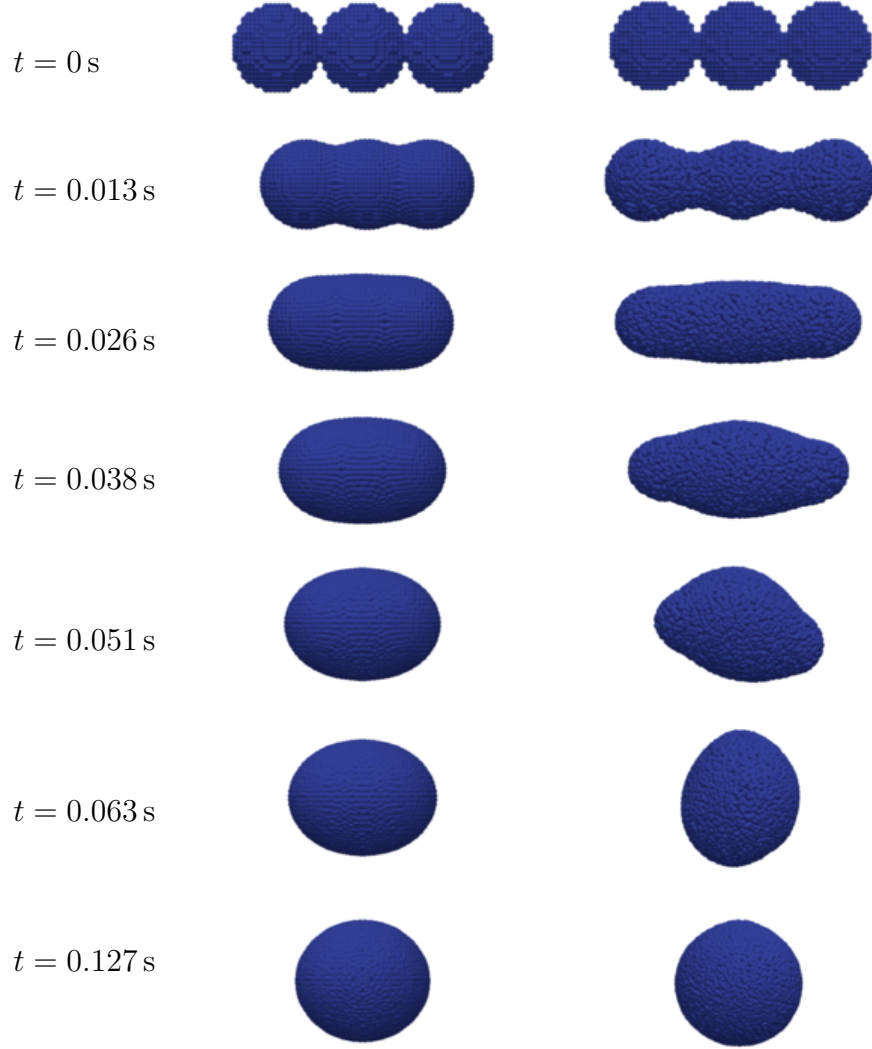


Figure 23: Comparison of the coalescence agglomerates. Left column shows the viscous flow assumption whereas the right column shows the melting process of initially solid particles.

References

- [1] Bonacina, C., Comini, G., Fasano, A., Primicerio, M. ., 1973. Numerical solution of phase-change problems. *Int. J. Heat Mass Transfer* 16 (10), 1825–1832.
- [2] Farrokhpanah, A., Bussmann, M., Mostaghimi, J., 2017. New smoothed particle hydrodynamics (sph) formulation for modeling heat conduction with solidification and melting. *Numerical Heat Transfer, Part B: Fundamentals* 71 (4), 299–312.
- [3] Gingold, R. A., Monaghan, J. J., 1977. Smoothed particle hydrodynamics - theory and application to non-spherical stars. *Mon. Not. R. Astron. Soc.* 181, 375–389.
- [4] Guo, N., Leu, M. C., 2013. Additive manufacturing: technology, applications and research needs. *Frontiers of Mechanical Engineering* 8 (3), 215–243.
- [5] Hsiao, J., Chung, B. T., 1986. An efficient algorithm for finite element solution to two-dimensional heat transfer with melting and freezing. *J. Heat Transfer* 108 (2), 462–464.
- [6] Hsiao, J.-S., 1983. Numerical and analytical analyses of heat transfer with ablation in a two-dimensional region. Ph.D. thesis, University of Akron.
- [7] Kirchhof, M., Schmid, H.-J., Peukert, W., 2009. Three-dimensional simulation of viscous-flow agglomerate sintering. *Physical Review E* 80 (2), 026319.
- [8] Kirchhof, M., Schmid, H.-J., Peukert, W., 2009. Three-dimensional simulation of viscous-flow agglomerate sintering. *Physical Review E* 80 (2), 026319.
- [9] Kreyszig, E., 2010. *Advanced engineering mathematics*. John Wiley & Sons.
- [10] Lucy, L. B., 1977. A numerical approach to the testing of the fission hypothesis. *Astronomical Journal* 82, 1013–1024.
- [11] May, D., Monaghan, J., 2003. Can a single bubble sink a ship? *American Journal of Physics* 71 (9), 842–849.
- [12] McCue, S. W., Wu, B., Hill, J. M., 2008. Classical two-phase stefan problem for spheres. In: *Proceedings of the Royal Society of London A: Mathematical, Physical and Engineering Sciences*. Vol. 464. The Royal Society, pp. 2055–2076.
- [13] Monaghan, J. J., 1992. Smoothed particle hydrodynamics. *Annual review of astronomy and astrophysics* 30, 543–574.

- [14] Morris, J. P., Fox, P. J., Zhu, Y., 1997. Modeling low reynolds number incompressible flows using sph. *J. Comput. Phys.* 136 (1), 214–226.
- [15] Nair, P., Pöschel, T., 2018. Dynamic capillary phenomena using incompressible sph. *Chemical Engineering Science* 176, 192–204.
- [16] Nair, P., Tomar, G., 2014. An improved free surface modeling for incompressible sph. *Comput. Fluids* 102, 304–314.
- [17] Nair, P., Tomar, G., 2015. Volume conservation issues in incompressible smoothed particle hydrodynamics. *Journal of Computational Physics* 297, 689–699.
- [18] Pasandideh-Fard, M., Mostaghimi, J., 1996. Droplet impact and solidification in a thermal spray process: droplet-substrate interaction. *Thermal spray: Practical Solutions for Engineering Problems*, CC Berndt (Ed.), Pub. ASM International, Material Park, Ohio-USA, 637–646.
- [19] Rowlinson, J. S., Widom, B., 2013. *Molecular theory of capillarity*. Courier Corporation.
- [20] Sleijpen, G. L., Van der Vorst, H. A., Fokkema, D. R., 1994. Bicgstab (l) and other hybrid bi-cg methods. *Numerical Algorithms* 7 (1), 75–109.
- [21] Stewartson, K., Waechter, R., 1976. On stefan’s problem for spheres. In: *Proceedings of the Royal Society of London A: Mathematical, Physical and Engineering Sciences*. Vol. 348. The Royal Society, pp. 415–426.
- [22] Szewc, K., Pozorski, J., Minier, J.-P., 2012. Analysis of the incompressibility constraint in the smoothed particle hydrodynamics method. *Int. J. Numer. Methods Eng.* 92 (4), 343–369.
- [23] Tartakovsky, A. M., Panchenko, A., 2016. Pairwise force smoothed particle hydrodynamics model for multiphase flow: surface tension and contact line dynamics. *J. Comput. Phys.* 305, 1119–1146.
- [24] Thomas, B., Samarasekera, I., Brimacombe, J., 1984. Comparison of numerical modeling techniques for complex, two-dimensional, transient heat-conduction problems. *Metallurgical and Materials Transactions B* 15 (2), 307–318.
- [25] Voller, V., Cross, M., 1981. Accurate solutions of moving boundary problems using the enthalpy method. *International journal of heat and mass transfer* 24 (3), 545–556.

- [26] Voller, V. R., Prakash, C., 1987. A fixed grid numerical modelling methodology for convection-diffusion mushy region phase-change problems. *Int. J. Heat Mass Transfer* 30 (8), 1709–1719.